

Direct Calculation of Wave Implosion for Detonation Initiation

Bao Wang,* Hao He,[†] and S.-T. John Yu[‡]
The Ohio State University, Columbus, Ohio 43202

Numerical simulations of imploding shock waves for detonation initiation are reported. We solve the one-dimensional Navier–Stokes equations and two-dimensional Euler equations for chemically reactive flows by the space–time conservation element and solution element method. One-dimensional results in cylindrical coordinates show that a converging shock produced by breaking a diaphragm for an initial pressure ratio of 1:0.2 atm is able to successfully initiate a detonation in an argon-diluted hydrogen/oxygen mixture ($0.2\text{H}_2 + 0.1\text{O}_2 + 0.7\text{Ar}$) initially at 300 K. The result also shows a two-shock implosion system caused by the interaction between the reflected primary shock and the imploding contact discontinuity. Two-dimensional solutions focus on imploding polygonal shock fronts. In each polygonal section, the imploding shock is analogous to a planar shock wave entering a channel with converging walls leading to complex wave reflections. Similar to that in the one-dimensional results, pressure histories in the focal region show multiple implosions.

I. Introduction

DETONATIONS could be easily initiated in a small initiator. Subsequent transmission of the detonation from the initiator to a larger chamber, however, requires suitable flow arrangement. In this setting, implosion could be useful to facilitate the transmission process. In the focal region, the collapsing shock front compresses the gas mixture adiabatically as it flows into a decreasing area, leading to a small region of extremely high energy density. In a successful arrangement, the compression would raise the postdetonation pressure to be higher than the Chapman–Jouguet (CJ) pressure, giving rise to an overdriven detonation wave. Such an effective shock-focusing mechanism could reduce the required sensitized initiator gas and the additional energy deposition for successful detonation transmission processes. Murray et al.¹ proposed the transmitting detonations from an initiator into a larger tube through various arrangements of annular orifices. Detonation waves, passing the annular orifice, generated imploding toroidal waves in the back of the orifice. Aided by high pressures and temperatures of imploding shocks, robust detonations could be reinitiated in the main chamber. Jackson et al.² and Jackson and Shepherd³ developed an imploding device by using an array of small channels. By merging multiple jets and wave fronts from the channels, they generated an imploding shock front in a circular chamber to detonate $\text{C}_3\text{H}_8/\text{air}$ mixtures.

Analytical solutions of imploding and exploding blast waves have been available in the self-similar regimes, approached by the evolving flows after the initial flow structure fades away. Based on dimensional analyses, classical solution of implosion was provided by Guderley.⁴ Self-similar solutions of explosion were developed by Taylor^{5,6} and Sedov.⁷ Later, these classical solution have been refined by Sharma and Radha,⁸ Toque,⁹ and van Dyke and Guttman.¹⁰ Other theoretical and experimental studies of imploding/exploding blast waves include Boyer,¹¹ Friedman,¹² Glass and Sisljan,¹³ Baker,¹⁴ and Schwendeman and Whitham.¹⁵

Many numerical simulations of implosions and explosions have been conducted. Brode^{16,17} reported simulations of spherical blast

waves. His numerical results were compared with an analytical solution based on an isothermal profile. In his numerical studies of detonation with a spherical charge of trinitrotoluene, he showed a second shock in the focal region. Flores and Holt¹⁸ employed Glimm's method¹⁹ to simulate explosions that were generated by a pressurized sphere in water. Charrier and Tessieras²⁰ studied a cylindrical explosion in air by using a front-tracking technique. Devore and Oran²¹ and Oran and DeVore²² used the flux-correction-transport (FCT) method^{23,24} and a connection machine to solve imploding detonation waves. Payne²⁵ used the Lax method²⁶ to simulate converging cylindrical shocks. Falcovitz and Birman²⁷ used the Godunov method²⁸ and studied various discontinuities in an explosion and implosion flow. Sod²⁹ proposed an operator splitting method to overcome the singularity problem at the focal center. He³⁰ used a second-order upwind method to simulate direct initiation of detonations. Menikoff et al.³¹ showed that it was important to resolve the curved detonation front and that a cell size on the order of 0.1 mm or less was required to resolve the reaction zone of common detonation waves.

The objective of present paper is to analyze the complex structures of converging shocks and the subsequent detonation initiation. We used the space–time conservation element and solution element (CESE) method^{32–41} to solve the one-dimensional Navier–Stokes equations and two-dimensional Euler equations for chemically reactive flows in cylindrical and Cartesian coordinates, respectively. In one-dimensional simulations, we focus on detonation initiation processes in an $\text{H}_2/\text{O}_2/\text{Ar}$ mixture. Chemical reactions are modeled by a finite-rate chemistry model composed of nine species and 24 reaction steps.⁴² Numerical results clearly show a multiple-implosion system caused by the interactions between the exploding shock reflected from the center and the imploding contact discontinuity. In two-dimensional calculations, we consider both reactive flow and nonreactive flows. For numerical efficiency, a global reaction model for $\text{C}_3\text{H}_8/\text{air}$ combustion⁴³ is employed. First, we consider circular imploding flows with small perturbations on the shock front. The perturbations are employed to mimic the effect of merging supersonic jets, similar to that by Jackson et al.,² and Jackson and Shepherd.³ We then consider implosion of several polygonal shock fronts. We use about 4.5 million mesh nodes in the two-dimensional calculations.

The rest of this paper is organized as follows. Section II provides the governing equations of the reactive flows. Section III presents the CESE method with numerical accuracy verification. Section IV illustrates the results and discussions. We then offer the conclusions.

II. Governing Equations

The one-dimensional Navier–Stokes equations for chemically reactive flows with N_s species are presented in the following

Received 1 July 2004; revision received 11 March 2005; accepted for publication 30 March 2005. Copyright © 2005 by the American Institute of Aeronautics and Astronautics, Inc. All rights reserved. Copies of this paper may be made for personal or internal use, on condition that the copier pay the \$10.00 per-copy fee to the Copyright Clearance Center, Inc., 222 Rosewood Drive, Danvers, MA 01923; include the code 0001-1452/05 \$10.00 in correspondence with the CCC.

*Graduate Research Assistant, Mechanical Engineering Department; wang.909@osu.edu. Student Member AIAA.

[†]Graduate Research Assistant, Mechanical Engineering Department; he.94@osu.edu. Student Member AIAA.

[‡]Associate Professor of Mechanical Engineering, Mechanical Engineering Department; yu.274@osu.edu. Member AIAA.

vector form:

$$\frac{\partial \mathbf{U}}{\partial t} + \frac{\partial \mathbf{F}(\mathbf{U})}{\partial r} + \frac{\partial \mathbf{F}_\mu(\mathbf{U})}{\partial r} = \mathbf{G}(\mathbf{U}) + \mathbf{S}(\mathbf{U}) \quad (1)$$

where r is the distance from the coordinate origin, t is time, \mathbf{U} is the flow variable vector, $\mathbf{F}(\mathbf{U})$ the inviscid flux vector, $\mathbf{F}_\mu(\mathbf{U})$ the viscous flux vector, $\mathbf{G}(\mathbf{U})$ the source term vector for nonplanar coordinates, and $\mathbf{S}(\mathbf{U})$ the source terms for chemical reactions:

$$\begin{aligned} \mathbf{U} &= (\rho, \rho u, \rho E, \rho_1, \rho_2, \dots, \rho_{N_s-1})^T \\ \mathbf{F} &= [\rho u, \rho u^2 + p, (\rho E + p)u, \rho_1 u, \rho_2 u, \dots, \rho_{N_s-1} u]^T \\ \mathbf{F}_\mu &= -(0, \tau_{rr}, \tau_{rr}u - q_r, \rho_1 \hat{u}_1, \rho_2 \hat{u}_2, \dots, \rho_{N_s-1} \hat{u}_{N_s-1})^T \\ \mathbf{G} &= -(1/r)[\rho u, \rho u^2 + \tau_{\theta\theta} - \tau_{rr}, (\rho E + p)u - \tau_{rr} \\ &\quad + q_r, \rho_1 u, \rho_2, \dots, \rho_{N_s-1} u]^T \\ \mathbf{S} &= (0, 0, 0, \dot{\omega}_1, \dot{\omega}_2, \dots, \dot{\omega}_{N_s-1})^T \end{aligned} \quad (2)$$

where ρ , u , p , E , and ρ_k are density, velocity, pressure, specific total energy, and density of species k , respectively. Density of the flow mixture ρ can be expressed by the summation of the species density:

$$\rho = \sum_{k=1}^{N_s} \rho_k \quad (3)$$

The specific total energy E is

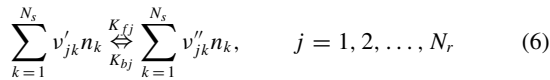
$$E = e + u^2/2 \quad (4)$$

where e is the specific internal energy of the gas mixture and it is calculated based on a mass-weighted average of the specific internal energy of each species e_k , that is,

$$e = \sum_{k=1}^{N_s} Y_k e_k \quad (5)$$

In Eq. (5), $Y_k = \rho_k/\rho$ is the mass fraction of species k . The specific internal energy e and the specific total energy E include the heat of formation of all species.

According to the law of mass action, a set of N_r reactions involving N_s species can be expressed by



where $n_k = \rho_k/W_k$ is the mole concentration of species k with W_k as the molecular weight of species k . In Eq. (6), v'_{jk} and v''_{jk} are the stoichiometric coefficients of species k in the j th reaction. The source term $\dot{\omega}_k$ in the k species equation is the summation of the generation rate of the species k from all chemical reactions involved,

$$\dot{\omega}_k = W_k \sum_{j=1}^{N_r} (\dot{n}_k)_j \quad (7)$$

where $(\dot{n}_k)_j$ is the generation rate of species k by reaction j :

$$(\dot{n}_k)_j = (v''_{jk} - v'_{jk}) \left(K_{fj} \prod_{l=1}^{N_s} n_l^{v'_{jl}} - K_{bj} \prod_{l=1}^{N_s} n_l^{v''_{jl}} \right) \quad (8)$$

The forward and backward reaction-rate constants K_{fj} and K_{bj} are formulated in the Arrhenius form:

$$\begin{aligned} K_{fj} &= A_{fj} T^{B_{fj}} \exp(-E_{fj}/R_u T) \\ K_{bj} &= A_{bj} T^{B_{bj}} \exp(-E_{bj}/R_u T) \end{aligned} \quad (9)$$

where A_f and A_b are the preexponential constants, E_f and E_b are the activation energies, and R_u is the universal gas constant. If the rate coefficients of the reverse reactions were unavailable, they can be calculated by using the equilibrium constant K_{eqj} :

$$K_{bj} = K_{fj}/K_{eqj} \quad (10)$$

where K_{eqj} can be determined by minimizing the free energy.

To proceed, the stress components in Eq. (2) are given as follows:

$$\tau_{rr} = \frac{2}{3} \mu \left(2 \frac{\partial u}{\partial r} - \frac{u}{r} \right) \quad (11)$$

$$\tau_{\theta\theta} = -\frac{2}{3} \mu \left(\frac{\partial u}{\partial r} - \frac{2u}{r} \right) \quad (12)$$

where the dynamic viscosity is calculated by using the Sutherland law,

$$\mu = \mu_0 \sqrt{\frac{T}{T_0}} \frac{1 + C/T_0}{1 + C/T} \quad (13)$$

The coefficients are $\mu_0 = 0.76813 \times 10^{-4}$, $T_0 = 1682.05$ K, and $C = 486.67$. These coefficients were obtained by fitting Eq. (13) with a series of viscosities of the reacting mixtures calculated by using the NASA Chemical Equilibrium with Applications (CEA) program⁴⁴ over a wide temperature range. The heat conduction and species diffusion are calculated by

$$q_r = -K \frac{\partial T}{\partial r} \quad (14)$$

$$\hat{u}_i = -\frac{D_{im}}{Y_i} \frac{\partial Y_i}{\partial r} \quad (15)$$

Instead of using complex mixing rules, we assume a constant Prandtl number $Pr = 0.72$ for calculating the heat conductivity and constant Schmidt number $Sc = 1.0$ for calculating the diffusion velocity \hat{u}_i for all specie involved.

For two-dimensional calculations, the Euler equations for chemically reactive flows are employed:

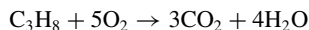
$$\frac{\partial u_m}{\partial t} + \frac{\partial f_m}{\partial x} + \frac{\partial g_m}{\partial y} = \mu_m \quad \text{with} \quad m = 1, 2, \dots, 5 \quad (16)$$

The flow variables $[u_m]$, the spatial fluxes $[f_m]$, $[g_m]$ and the source term $[\mu_m]$ are

$$\begin{aligned} [u_m] &= \begin{pmatrix} \rho \\ \rho u \\ \rho v \\ \rho E \\ \rho_f \end{pmatrix}, & [f_m] &= \begin{pmatrix} \rho u \\ \rho u^2 + p \\ \rho uv \\ (\rho E + p)u \\ \rho_f u \end{pmatrix} \\ [g_m] &= \begin{pmatrix} \rho v \\ \rho uv \\ \rho v^2 + p \\ (\rho E + p)v \\ \rho_f v \end{pmatrix}, & [\mu_m] &= \begin{pmatrix} 0 \\ 0 \\ 0 \\ 0 \\ \dot{\omega}_f \end{pmatrix} \end{aligned} \quad (17)$$

All flow variables are defined in the same way as those in the one-dimensional case except additional y coordinate and the y component velocity v . Because we only consider a one-step finite-rate reaction for the C_3H_8 /air mixture, the chemical composition of the gas mixture could be readily calculated if the concentration of the fuel, that is, propane, is known. Thus we only include one species equation in the model when there are four chemical species in the

single-step reaction. The finite-rate reaction model is taken from Dryer⁴³:



$$\frac{d}{dt} [\text{C}_3\text{H}_8] = -A \exp\left(-\frac{E_a}{R_u T}\right) [\text{C}_3\text{H}_8]^a [\text{O}_2]^b \quad (18)$$

The coefficients in the preceding rate equation are $A = 8.6 \times 10^{11}$, $E_a = 30$, $a = 0.1$, and $b = 1.65$. Units are cm-sec-mole-Kcal-K.

III. CESE Method

In the present work, the space-time CESE method, originally proposed by Chang³⁸ and Chang et al.,^{39,40} is employed. Previously, we have extended the CESE method for chemically reactive flows^{32–36} with comprehensive finite-rate kinetics and thermodynamics models. The CESE method is distinguished by the simplicity of its design principle, that is, a unified treatment of space and time in calculating flux conservation. In contrast to modern upwind methods, the CESE method does not use a Riemann solver or a reconstruction procedure as the building blocks of the numerical algorithm. Therefore, the logic and operation count of the CESE method are much simpler. They are comparable to a straightforward central differencing scheme. The details of the CESE method have been extensively illustrated in Refs. 38–40. In the present paper, only a brief discussion of the essential steps of the CESE method is provided.

To introduce the advantageous space-time-integration formulation of the CESE method, we first discuss the conventional finite volume methods, in which, because space and time are not treated equally, the choices of the space-time geometry of the finite volume have been restricted. As a result, the Riemann problem is unavoidable in calculating the space-time flux. Thus, the use of an efficient Riemann solver in modern upwind schemes became a paradigm in shock-capturing schemes. We will then show that, because of a unified treatment of space and time, the CESE formulation allows flexible choices of space-time geometry in calculating fluxes such that the Riemann problem is totally avoided. Moreover, the spatial gradients of the flow variables are treated as the unknowns, and they march in time with the flow variables. Thus the reconstruction step is eliminated in the CESE method.

A. Finite Volume Methods

Consider the following convection equation:

$$\frac{\partial u}{\partial t} + \frac{\partial f}{\partial x} = \tau(u) \quad (19)$$

where u is the density of the substance, f is the spatial flux, and $\tau(u)$ is the source term. According to the Reynolds transport theorem, we have the integral equation

$$\frac{\partial}{\partial t} \int_V u dV = - \int_{S(V)} f \cdot d\mathbf{S} + \int_V \tau(u) dV \quad (20)$$

Equation (20) states that the rate of change of the total amount of a substance contained in a spatial domain V is equal to the combined effect of 1) the flux of that substance across the boundary of V , that is, $S(V)$, and 2) the source term integration over V . The conventional finite volume methods concentrated on calculating the flux through $S(V)$. The time-derivative term is usually treated by a finite difference method, for example, the Runge-Kutta method. Or integration can be performed for temporal evolution:

$$\int_V u dV \Big|_{t_1}^{t_2} = \int_{t_1}^{t_2} \left[- \int_{S(V)} f \cdot d\mathbf{S} + \int_V \tau(u) dV \right] dt \quad (21)$$

In this setting, the space-time domain in one spatial dimension must be rectangular. Refer to Fig. 1a. The unknowns are usually placed at the center of the spatial mesh, that is, on the boundary of the finite volume (FV). The FVs must be stacked up exactly on the top of each other in the temporal evolution direction. For equations in two

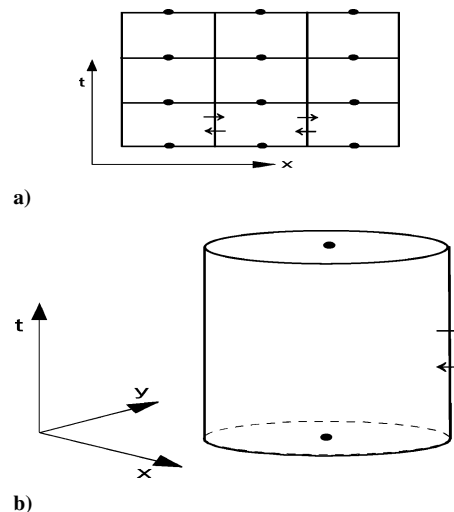


Fig. 1 Space-time integration for conventional finite volume methods in one and two spatial dimensions.

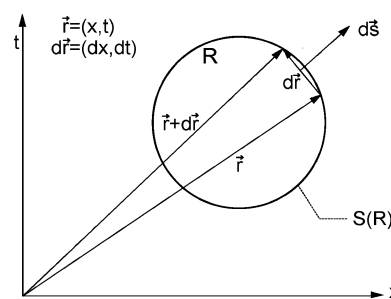


Fig. 2 Schematic of the space-time integral.

spatial dimensions, as depicted in Fig. 1b, a FV is a uniform-cross-section cylinder in the space-time domain. Again, no staggering in time is allowed. This arrangement results in vertical interfaces extended in the direction of time evolution between adjacent FVs. Across the interfaces, flow information travels in both directions. Therefore, an upwind-biased method (or a Riemann solver) must be employed to calculate the flux.

B. Space-Time Integration

To treat the same convection equation (19) according to the CESE method, we let $x_1 = x$ and $x_2 = t$ be the coordinates of a two-dimensional Euclidean space E_2 . Equation (19) becomes

$$\nabla \cdot \mathbf{h} = \tau(u) \quad (22)$$

where the current density vector

$$\mathbf{h} = (au, u) \quad (23)$$

By using Gauss's divergence theorem in E_2 , Eq. (22) becomes

$$\oint_{S(R)} \mathbf{h} \cdot d\mathbf{s} = \int_R \tau(u) dR \quad (24)$$

where $S(R)$ is the boundary of an arbitrary space-time region R in E_2 , $d\mathbf{s} = d\sigma \mathbf{n}$ with $d\sigma$ and \mathbf{n} , respectively, being the area and the outward unit normal of a surface element on $S(R)$, and dR is the volume of a space-time region inside $S(R)$. In Eq. (24), $\mathbf{h} \cdot d\mathbf{s}$ is the space-time flux of \mathbf{h} leaving the region R through the surface element $d\mathbf{s}$. Figure 2 is a schematic of Eq. (24). There is no restriction on the space-time geometry of the conservation elements, over which Eq. (24) is enforced. In what follows, we briefly illustrate the numerical integration of Eq. (24).

To proceed, let Ω denote the set of all staggered space-time mesh nodes (j, n) in E_2 (dots in Fig. 3a) with n being a half or whole

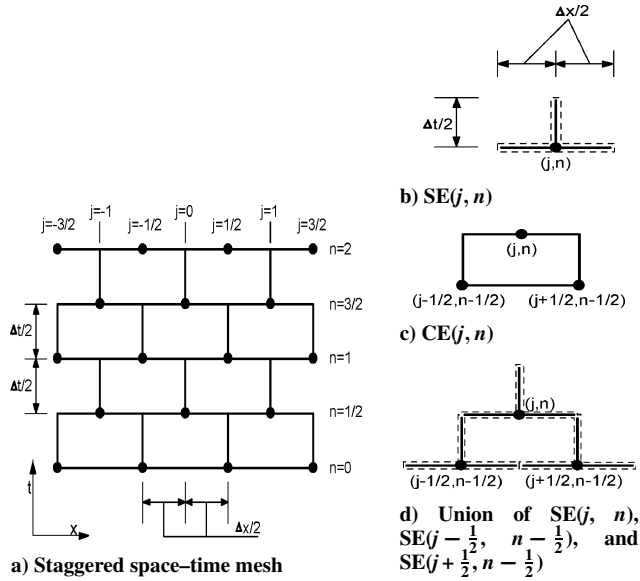


Fig. 3 Space-time mesh of the CESE method:

integer, and $(j - n)$ being a half-integer. For each $(j, n) \in \Omega$, let the solution element $SE(j, n)$ be the interior of the space-time region bounded by a dashed curve depicted in Fig. 3b. It includes a horizontal line segment, a vertical line segment, and their immediate neighborhood. The exact size of this neighborhood does not matter. For any $(x, t) \in SE(j, n)$, let $u(x, t)$ and $\mathbf{h}(x, t)$, respectively, be approximated by $u^*(x, t; j, n)$ and $\mathbf{h}^*(x, t; j, n)$. We define $u^*(x, t; j, n)$ by

$$u^*(x, t; j, n) = u_j^n + (u_x)_j^n (x - x_j) + (u_t)_j^n (t - t^n) \quad (25)$$

where 1) u_j^n , $(u_x)_j^n$, and $(u_t)_j^n$ are constants in $SE(j, n)$ and 2) (x_j, t^n) are the coordinates of the mesh point (j, n) . To simplify the discussion of the numerical algorithm, we let $f = au$ with a as a constant. Furthermore, we let

$$(u_t)_j^n = -a(u_x)_j^n \quad (26)$$

in Eq. (25). To justify Eq. (26), we assume that the value of u on a macroscale [that is, the value of u obtained from an averaging process involving a few neighboring conservation elements (CEs)] does not vary significantly as a result of redistribution of the source term τ over each CE, over which Eq. (24) must be satisfied. As such, we take the liberty to redistribute the source term such that all source-term effects associated with each mesh node will be calculated in a rectangle attached to the bottom of the corresponding SE. Thus, there is no source-term effect along the vertical line segment of each SE. Please refer to Ref. 32 for detailed discussions of treating source terms in the CESE method. Aided by Eq. (26), Eq. (25) becomes

$$u^*(x, t; j, n) = u_j^n + (u_x)_j^n [(x - x_j) + a(t - t^n)] \quad (27)$$

$(x, t) \in SE(j, n)$

There are two marching variables u_j^n and $(u_x)_j^n$ associated with each $(j, n) \in \Omega$. Furthermore, because $\mathbf{h} = (au, u)$, we have

$$\mathbf{h}^*(x, t; j, n) = [au^*(x, t; j, n), u^*(x, t; j, n)] \quad (28)$$

Let E_2 be divided into nonoverlapping rectangular regions referred to as conservation elements. Shown in Fig. 3c, the CE with the midpoint of its top face being any mesh point $(j, n) \in \Omega$ is denoted by $CE(j, n)$. The discrete approximation of Eq. (24) is

$$\oint_{S[CE(j,n)]} \mathbf{h} \cdot \mathbf{ds} = \tau(u_j^n) \times \frac{\Delta x \Delta t}{2} \quad (29)$$

Here $\tau(u_j^n)$ is the average value of $\tau(u)$ in $CE(j, n)$. Because $(\Delta x \Delta t)/2$ is the volume of $CE(j, n)$, Eq. (29) simply states that

the total space-time flux of \mathbf{h}^* leaving the boundary of any CE is equal to the source-term integration over the CE. Because the surface integration over any interface separating two neighboring CEs is evaluated using the information from the same SE, the local flux conservation relation Eq. (29) leads to global flux conservation.

Without going into details, the boundary of $CE(j, n)$ is a subset of the union of $SE(j, n)$, $SE(j - \frac{1}{2}, n - \frac{1}{2})$ (refer to Fig. 3d), and Eqs. (27–29) imply that

$$u_j^n - (\Delta t/2)\tau(u_j^n) = \frac{1}{2} \left[(1 - v)u_{j+\frac{1}{2}}^{n-\frac{1}{2}} - (1 - v^2)(u_x^+)_j^{n-\frac{1}{2}} + (1 + v)u_{j-\frac{1}{2}}^{n-\frac{1}{2}} + (1 + v^2)(u_x^-)_j^{n-\frac{1}{2}} \right] \quad (30)$$

Here, 1) $v \equiv (a\Delta t)/\Delta x$ is the Courant number and 2) $(u_x^\pm)_j^n \equiv (\Delta x/4)(u_x)_j^n$, $(j, n) \in \Omega$ is the normalized form of $(u_x)_j^n$. Given the values of the marching variables at the $(n - \frac{1}{2})$ th time level, u_j^n is determined by solving Eq. (30) with the aid of Newton's iteration method. The initial condition for Newton's iterations is calculated by assuming that the source term is zero. After u_j^n is known, $(u_x^\pm)_j^n$ is evaluated using an oscillation-suppressing procedure,^{39,40} which is briefly illustrated in the following. Aided by Eq. (26), we perform Taylor expansion in time and have

$$u_{j\pm\frac{1}{2}}^n \equiv u_{j\pm\frac{1}{2}}^{n-\frac{1}{2}} + (\Delta t/2)(u_t)_{j\pm\frac{1}{2}}^{n-\frac{1}{2}} \equiv u_{j\pm\frac{1}{2}}^{n-\frac{1}{2}} - 2v(u_x^\pm)_{j\pm\frac{1}{2}}^{n-\frac{1}{2}} \quad (31)$$

According to Eq. (31), $u_{j\pm\frac{1}{2}}^n$ is a first-order Taylor's approximation of u at $(j \pm \frac{1}{2}, n)$. Let

$$(u_x^\pm)_j^n \equiv \pm (u_{j\pm\frac{1}{2}}^n - u_j^n) = \pm \frac{\Delta x}{4} \frac{u_{j\pm\frac{1}{2}}^n - u_j^n}{\Delta x/2} \quad (32)$$

where $(u_{x+}^+)_j^n$ and $(u_{x-}^+)_j^n$, aside from a normalized factor $\Delta x/4$, are two numerical analogs of $\partial u/\partial x$ at (j, n) with one being evaluated from the right and the other evaluated from the left. Let the reweighting function W be defined by 1) $W(0, 0, \alpha) = 0$ and 2)

$$W(x_-, x_+, \alpha) = \frac{|x_-|^\alpha x_- + |x_+|^\alpha x_+}{|x_-|^\alpha + |x_+|^\alpha} \quad (33)$$

Then $(u_x^\pm)_j^n$ is calculated using

$$(u_x^\pm)_j^n = W \left[(u_{x+}^+)_j^n, (u_{x-}^+)_j^n, \alpha \right] \quad (34)$$

In all calculations, we let $\alpha = 1$.

C. Numerical Accuracy Verification

Two one-dimensional cases are presented to assess the numerical accuracy of the computer codes. First, we report the numerical result of an expanding cylindrical shock. The one-dimensional Euler equations in a cylindrical coordinate, a subset of Eq. (2.1), for nonreacting flows are solved. The initial conditions of the cylindrical shock are taken from Toro⁴⁵:

$$\begin{aligned} P_{\text{in}} &= 1.0 & P_{\text{out}} &= 0.1 \\ \rho_{\text{in}} &= 1.0, & \rho_{\text{out}} &= 0.125 \\ u_{\text{in}} &= 0.0 & u_{\text{out}} &= 0.0 \end{aligned} \quad (35)$$

Subscripts in and out denote values inside and outside the circular discontinuity. The initial radius for the shock is 0.4. As shown in Fig. 4, by using only 100 cells the snapshots of flow properties at time $t = 0.25$ agree well with the results obtained by using Glimm's method¹⁹ with 1000 cells.⁴⁵

Next, we consider Sedov's analytical solution⁷ of an expanding blast wave in an ideal gas with the specific heat ratio $\gamma = 1.4$ and the molecular weight 28.98. For the undisturbed gas, density $D_1 = 1.25 \text{ kg/m}^3$, temperature $T_1 = 293 \text{ K}$, and the initially deposited total energy is 1300 J. The self-similar solution by Sedov at time $t = 2.8 \times 10^{-6} \text{ s}$ is used as the initial condition. Figure 5 shows the calculated snapshots of the flow profile compared with Sedov's analytical solution after a short period of time $\Delta t = 1.92 \times 10^{-8} \text{ s}$.

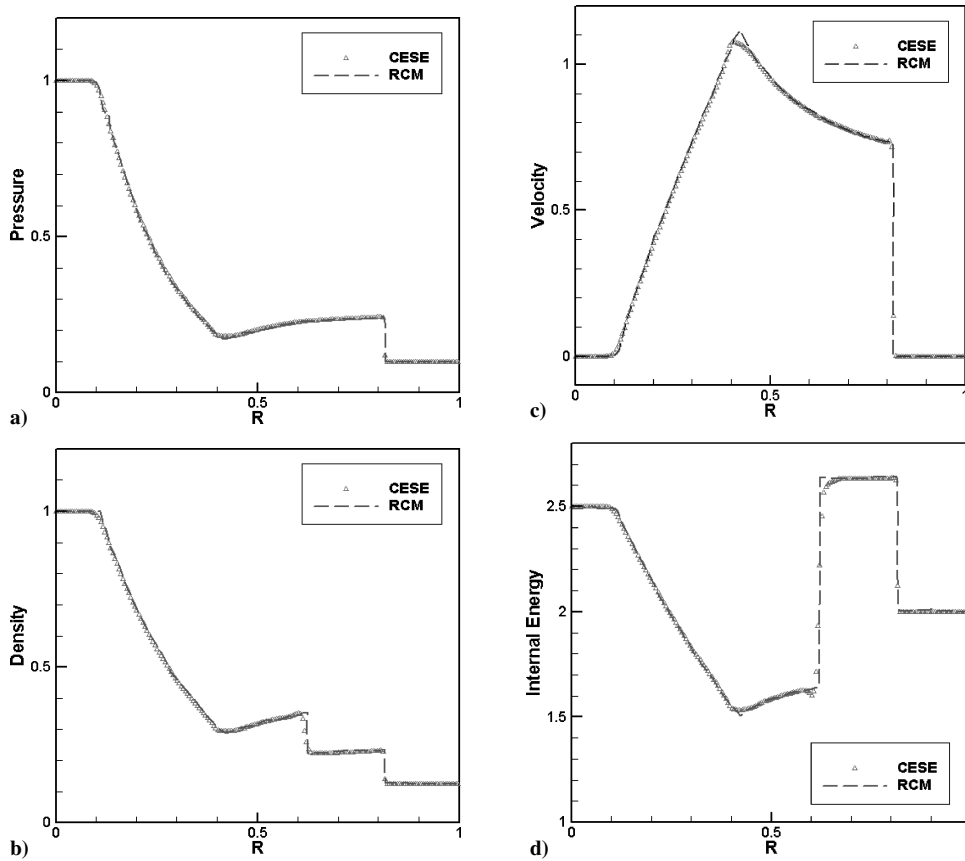


Fig. 4 CESE results compare with the solutions⁴⁵ by the RCM method for a cylindrical expanding shock: a) pressure, b) density, c) velocity, and d) specific internal energy.

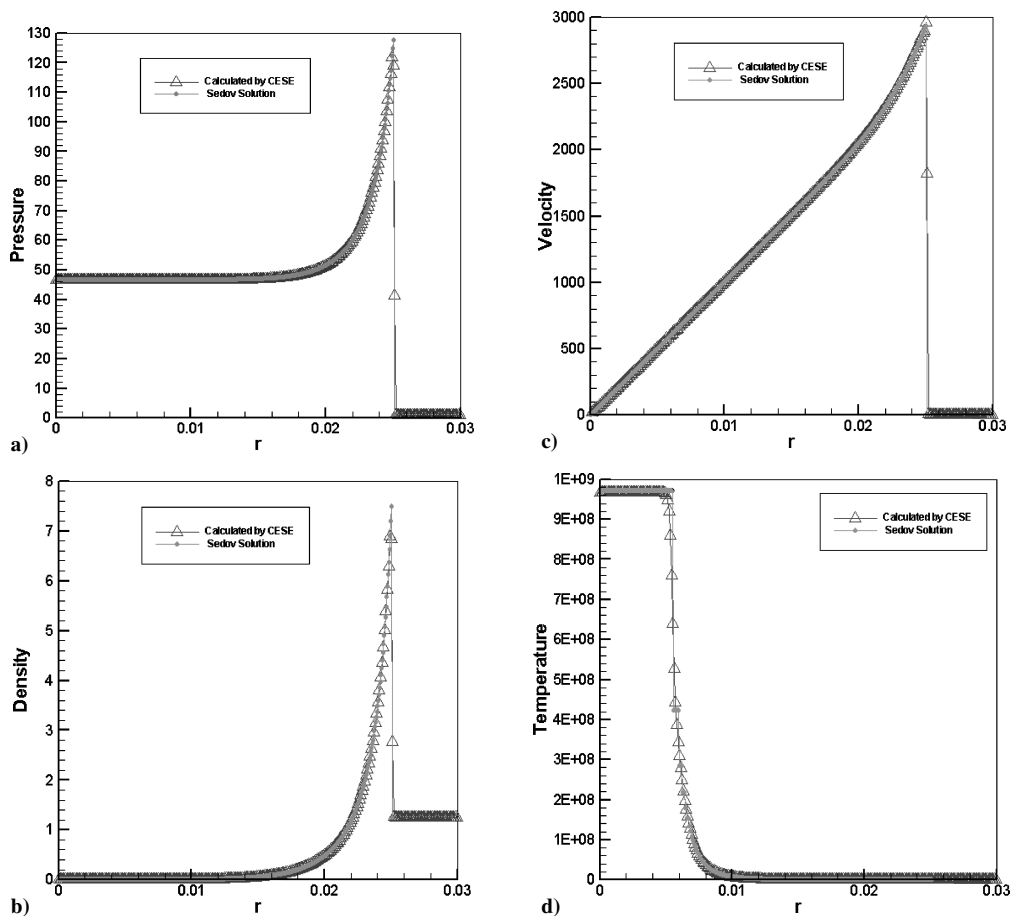


Fig. 5 CESE results compared with Sedov's analytical solutions for an explosion problem: a) pressure, b) density, c) velocity, and d) temperature.

IV. Results and Discussion

A. One-Dimensional Results

To set up the imploding shock, the initial conditions are composed of two regions separated at $r = r_0$. We let $r_0 = 0.1$ m, and the computational domain is $0 < r < 0.38$ m. We use 28,800 equally spaced mesh nodes for the entire computational domain. To maintain numerical stability, the time-step size is dynamically adjusted to maintain the maximum Courant–Friedrichs–Lewy (CFL) number ≈ 0.5 . Moreover, the CFL insensitive scheme⁴¹ has been employed to minimize the artificial damping caused by the wide range of CFL numbers in the computational domain.

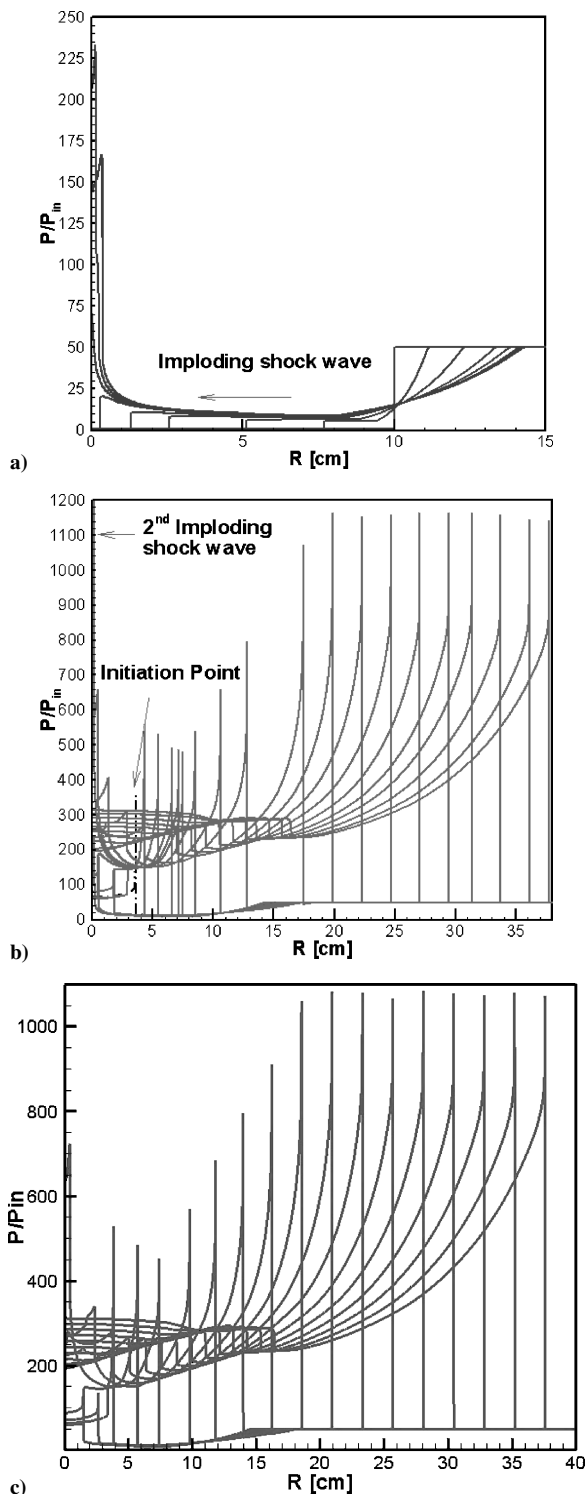


Fig. 6 Pressure profiles at various times for the case of $P_{out}/P_{in} = 50$: a) implosion, b) explosion, and c) implosion/explosion with 14,400 cells.

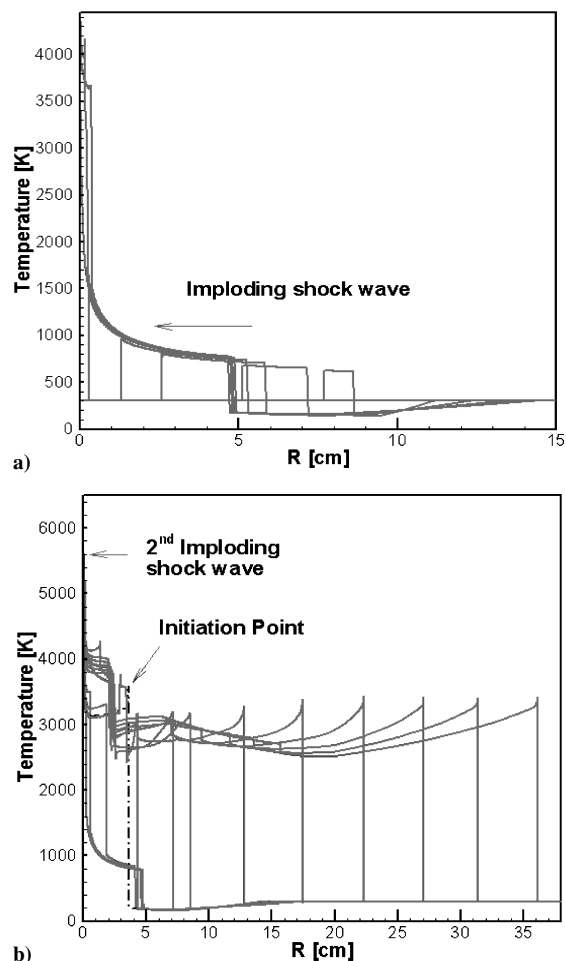


Fig. 7 Temperature profiles at various times for $P_{out}/P_{in} = 50$: a) implosion and b) explosion.

Two cases are considered. For both cases, the initial mole concentration ratio of the $H_2/O_2/Ar$ gas mixture is 2:1:7, and the initial temperature of the whole domain is 300 K. In the first case, the pressure ratio is 50:1. The initial pressure of the driving region, where $r > r_0$, is $P_{out} = 10$ atm, and the initial pressure of the driven region $P_{in} = 0.2$ atm. In the second case, the pressure ratio is 5:1 with $P_{out} = 1$ atm and $P_{in} = 0.2$ atm.

For the first case with the initial pressure ratio of 50:1, Figs. 6–9 show the calculated pressure, temperature, density, and velocity profiles at different times. Note that the values of the preceding flow variables in the implosion phase are significantly different from those in the exploding phase. Therefore, two plots are provided for each flow variable: one for the imploding phase and the other for the exploding phase. Figure 6c is an additional pressure plot in the exploding phase calculated by using a coarser mesh of 14,400 mesh nodes. Figure 6c is almost identical to Fig. 6b. This result shows that the present flow solutions are mesh-independent.

When the diaphragm separating the driving and driven sections is lift, the primary shock wave, followed by a contact discontinuity, implodes to the center. In the opposite direction, a rarefaction wave moves away from the center. In the imploding phase, pressure and velocity behind the imploding shock steadily increase as a result of the decreasing area. After reflection from the center, the main shock moves outward and clashes with the imploding contact discontinuity. The strength of the main shock is greatly enhanced by the interaction. It penetrates through the contact discontinuity, catches up with the expansion wave, and quickly develops to be a robust detonation wave at about $r = 20$ cm.[§]

[§]Please refer to <http://cfd.eng.ohio-state.edu/imp-exp.htm> for animation of the evolving solutions.

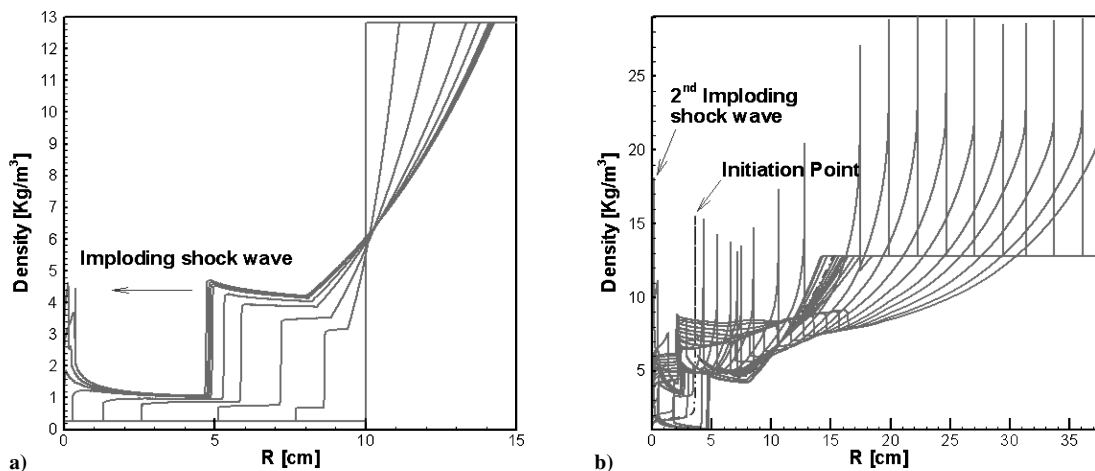


Fig. 8 Density profiles at various times for $P_{out}/P_{in} = 50$: a) implosion and b) explosion.

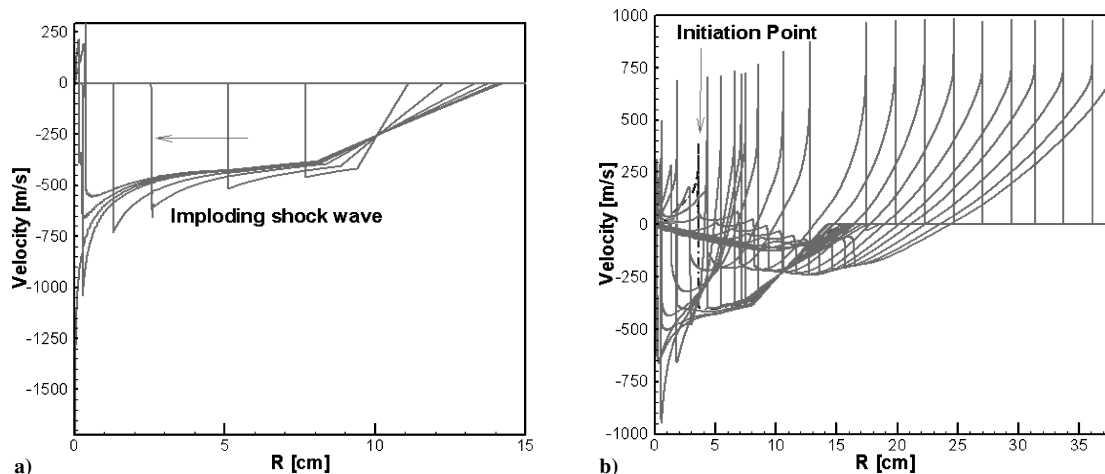


Fig. 9 Velocity profiles at various times for $P_{out}/P_{in} = 50$: a) implosion and b) explosion.

Figure 10 shows the space–time records of pressure, density, temperature, velocity, and the OH mass fraction. The interaction between the exploding shock and the imploding contact discontinuity creates a new shock wave at the collision point, and this secondary shock implodes to the center. The same interaction only slightly slows down the discontinuity wave in its imploding motion. The implosion of the second shock raises the pressure and temperature in the focal point even higher. Similar to the main shock, the reflected second shock collides with the contact discontinuity wave again and generates the third imploding shock, which is much weaker but discernible in Figs. 10b and 10d. After the collision, the reflected secondary shock penetrates the contact discontinuity wave and continues moving outwardly. After interacting with the reflected secondary shock, the contact discontinuity stops the inward motion and becomes stationary at about $r = 2$ cm. This stationary contact discontinuity wave could be seen as a vertical line along $r = 2$ cm in Figs. 10b and 10d. Similar to the main shock and the secondary shock, the third shock implodes inwardly, reflects from the focal point, and collides with the contact discontinuity wave. However, details are too weak to be observed in Fig. 10.

Figure 11 shows the distribution of the H_2 mass fraction profile in the reaction zone of the detonation wave. The half-reaction zone, defined as the distance from the leading shock to the position where a half of the fuel has been consumed, is approximately 1.6×10^{-4} m, and it is resolved by 13 mesh points. In our previous work,³⁶ we solved the classical Zeldovich, von Neuman, and Doering (ZND) model equations with an one-step global reaction by the CESE method. We showed that four to five points per half-reaction zone are enough to achieve accurate resolution of the classical ZND

detonation wave. The size of the reaction zone and the associated mesh resolution used in the present paper are typical. For example, Lu et al.⁴⁶ showed that the induction zone of their detonation in a stoichiometric hydrogen/air mixture initially at 1 atm and 298 K is about 2×10^{-4} m. By using the ENO method,⁴⁷ Hwang et al.⁴⁸ used 20 mesh points to resolve a half-reaction zone of a detonation wave.

Figure 12 shows the space–time trajectories of the main shocks in the two cases. Near the focal point, the trajectories of the imploding/exploding shocks of both cases deviate from the straight lines, which are denoted by the dashed lines representing the CJ detonations. During the implosion phase of the flows, the slopes of two imploding shock trajectories are markedly different because of different shock strengths. In the exploding phase, however, two shock trajectories have nearly identical slopes. In both cases, detonations have been successfully initiated when $t > 300 \mu s$, and they propagate at their CJ velocities, at about 1652 m/s, to the far field. We remark that more heat is released in the $P_{out}/P_{in} = 50$ case because of higher pressure at the driven section. Nevertheless, the detonation speeds of the two cases are about the same because the pressure ratios across the detonation waves are similar. This has been verified by comparison with the thermodynamics calculations by using the CEA program.⁴⁴

For additional mesh refinement tests, Fig. 13 shows two trajectories of the primary shock of the $P_{out}/P_{in} = 50$ case, calculated by using 14,400, and 28,800 mesh nodes, corresponding to $\Delta x = 0.028$ and 0.014 mm, respectively. The shock speed in the implosion phase for the $P_{out}/P_{in} = 50$ case is further verified by comparison with the classical solution in Table 1 (Refs. 4 and 49–53). In Fig. 14, we replot the trajectory of converging shock of the

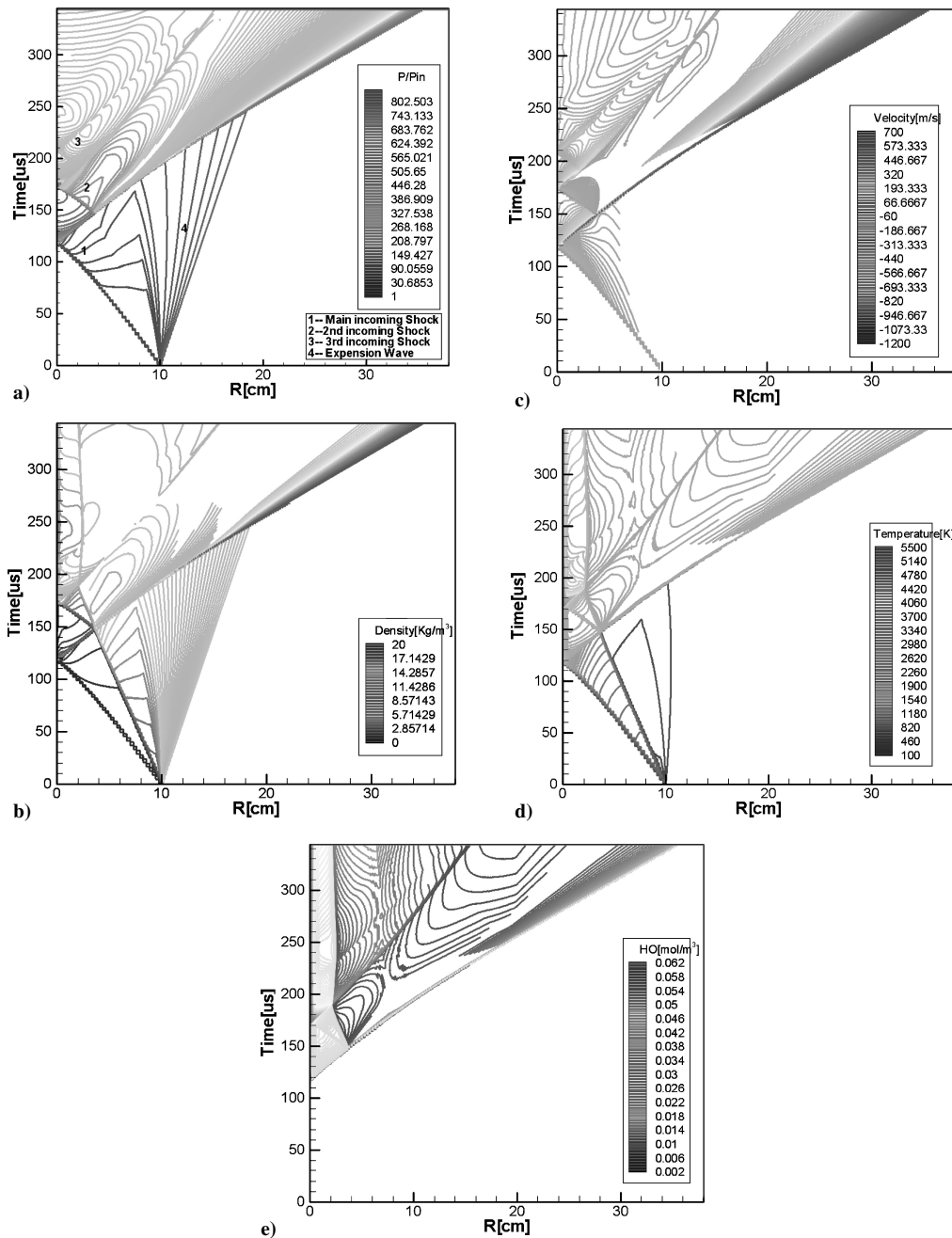


Fig. 10 Space-time records of flow variables for the case of $P_{out}/P_{in} = 50$: a) pressure, b) density, c) velocity, d) temperature, and e) mass fraction of OH.

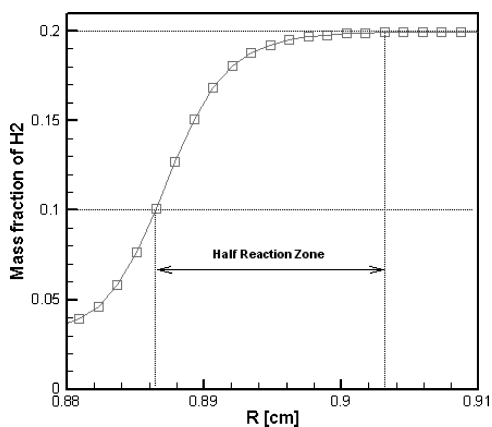


Fig. 11 Numerical resolution of the reaction zone for the case of $P_{out}/P_{in} = 50$.

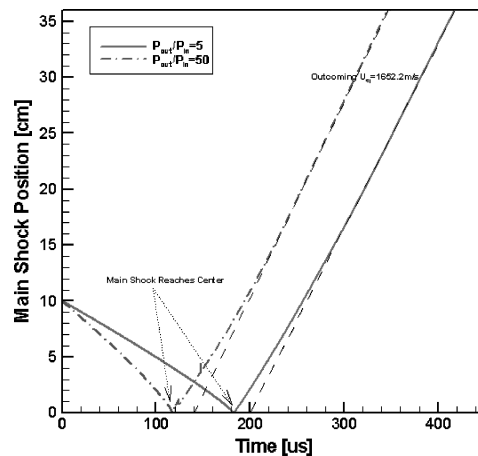


Fig. 12 Space-time trajectories of the main shocks of the $P_{out}/P_{in} = 5$ and $P_{out}/P_{in} = 50$ cases.

Table 1 Exponent in the self-similar solution of an imploding wave

References	Self-similar exponent α	Mach number
CESE (2004)	0.835	2.1
Guderley (1942) ⁴	0.834	—
Butler (1954) ⁴⁹	0.835217	—
Sanyukovich (1960) ⁵⁰	0.834	—
De Neef and Nechtman (1978) ⁵¹	0.835 ± 0.003	—
Takayama et al. (1984) ⁵²	0.831 ± 0.002	$M_s = 1.1-2.1$
Kleine (1985) ⁵³	0.832 ± 0.028	$M_s = 1.3-2.1$

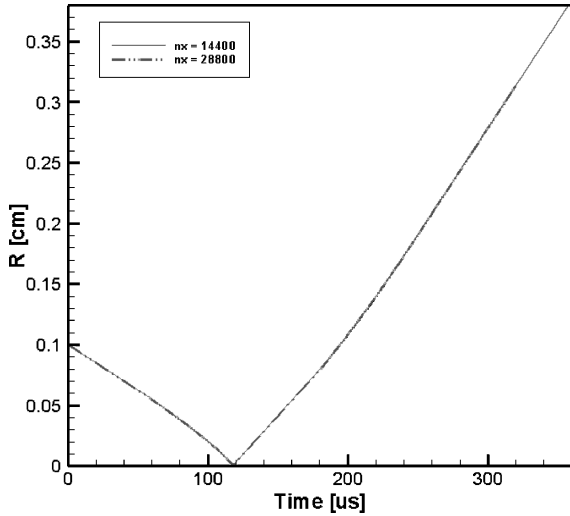


Fig. 13 Shock front locations from grid study.

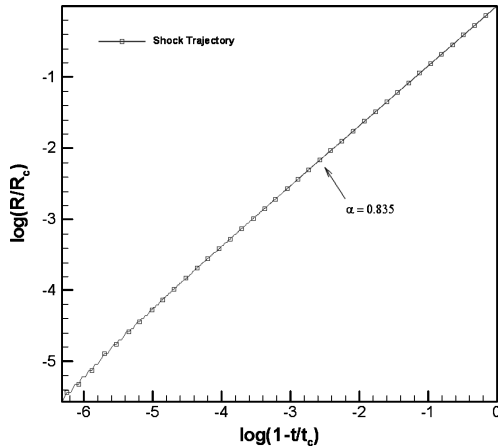


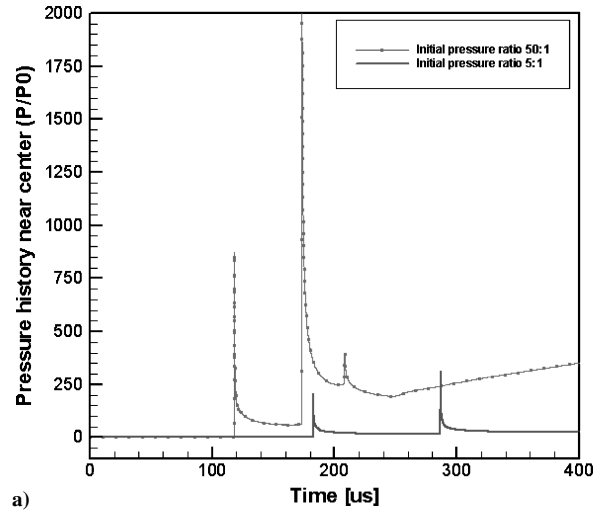
Fig. 14 Shock trajectory of imploding shocks with an initial Mach number of 2.1.

$P_{out}/P_{in} = 50$ case based on Sedov's asymptotic relation⁷:

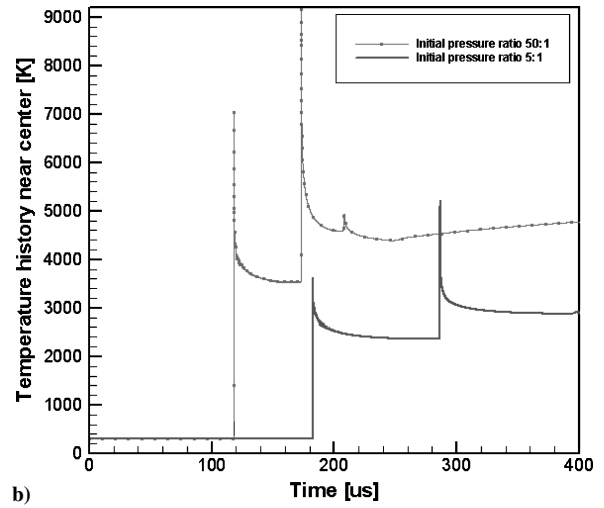
$$R/R_c = (1 - t/t_c)^\alpha \quad (36)$$

where R_c is the radius of the starting converging shock and t_c the time when the converging shock arrives the center. In Fig. 14, the x axis is $\log(1 - t/t_c)$, and the y axis is $\log(R/R_c)$. Based on Eq. (36), the trajectory is a straight line with the slope equal to α . In our calculation, we found that the shock trajectory of the $P_{out}/P_{in} = 50$ case is indeed a straight line with $\alpha = 0.835$ except in the region near the center. We note that for this case, the initial Mach number of the imploding shock is 2.1.

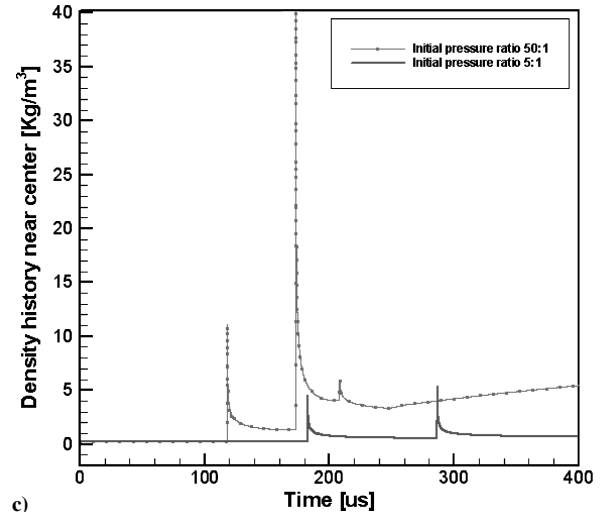
Figure 15 shows the histories of temperature, pressure, and density at the focal point of the implosion/explosion process. For $P_{out}/P_{in} = 50$, the presence of the third implosion wave can be clearly seen. For $P_{out}/P_{in} = 5$, the third implosion is too weak to be detected. In both cases, maximum flow variables are achieved by



a)



b)



c)

Fig. 15 Time histories at the focal point for $P_{out}/P_{in} = 5$ and $P_{out}/P_{in} = 50$: a) pressure, b) temperature, and c) density.

the implosion of the second shock. The pressure values are normalized by the initial pressure P_{in} of the driven gases.

B. Two-Dimensional Results

For two-dimensional calculations of implosions and explosions, we consider a circular computational domain. Figure 16 is a schematic of the computational domain and the associated mesh. Because of flow symmetry, the actual computational domain is a quarter of the shown circular domain. All calculations to be presented use

the same mesh, which is composed of about 4.5 million quadrilaterals. In all calculations, the initial condition includes two separate regions with $P_{\text{out}}/P_{\text{in}} = 20$ and $P_{\text{in}} = 0.2$ atm. Temperature is uniform at 300 K for the whole domain and $\rho_{\text{out}}/\rho_{\text{in}} = 20$.

Four implosion cases are presented. Three of them are nonreacting flows of 1) a square front, 2) an octagonal front, and 3) a circular front with sinusoidal perturbations in pressure. In the third case, the amplitude of the perturbation is 2% of the initial pressure difference between the driver and driven sections. We impose 32 cycles of sinusoidal perturbations around the circular front. The fourth implosion case is a reacting circular shock front with similar perturbations. In all cases, the radius of the computational domain $R = 0.38$ m. In the first case of the square diaphragm, the length of each side of the initial shock front is 0.38 m. For the octagonal diaphragm, the length

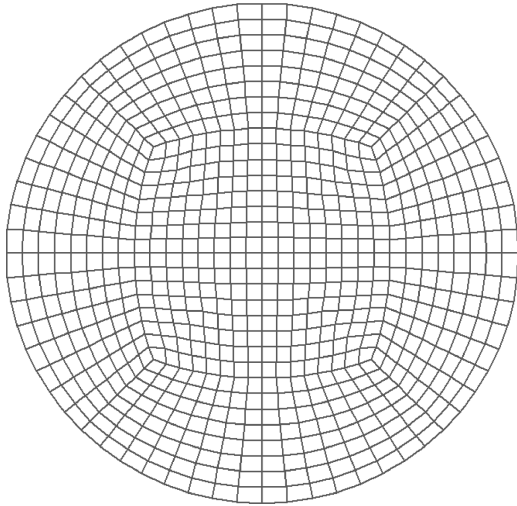


Fig. 16 Schematic of the mesh for two-dimensional implosion. A quarter of the circular domain is calculated, and mesh size is composed of about 4.5 million quads.

of each edge is 0.204 m, and the distance from the center to each vertex is 0.266 m. For the circular diaphragm with perturbations, the radius of the circle is 0.253 m or $\frac{2}{3}R$.

Figures 17–19 show snapshots of pressure contours at various time steps for the just-mentioned three nonreactive cases. Each time unit is about 1.3 ms. In each case, flow evolution is symmetric with respect to the bisector of each vertex of the polygon. In other words, the bisectors behave like inviscid walls. Evolution of each side of a polygonal shock front can be interpreted as a planar shock entering into a channel of convergent walls or a wedge-shaped cavity. Imploding shocks interact with the bisector and form Mach reflection. In general, the evolution of each planar section of the polygonal shock front resembles the scenario of a shock-on-wedge problem, in which an incident shock interacts with a wedge with the bisector corresponding to a wedge surface. In this process, the Mach stem of the Mach reflection propagates with a wave speed faster than that of the initial shock. As a result, the Mach stem increases in size, while the length of the shock front decreases to zero. During this evolution, the number of the vertices of the imploding polygon doubles that of the initial polygon. Finally, a new polygon is formed with a similar shape, but the orientation is rotated. Seemingly, the original polygon, with a shrunk area, was recovered with a rotated orientation. The sides of this smaller polygon are composed of Mach stems. However, it is known that Mach stems are curved. Thus, the regenerated polygonal shocks have curved sides. One can have multiple regenerations of the polygonal front during the imploding process.

Figure 20 shows the time histories of temperature and pressure at the focal region for three nonreacting cases. The dimensionless temperature in Fig. 20 is defined as T/T_{in} , that is, each unit is 300 K. For the pressure curve, the dimensionless P/P_{in} , that is, each unit is 0.2 atm. The x axis is dimensionless time. Each unit is about 1.3 ms.

The case of square front has lower maximum pressure and temperature because of stronger Mach reflections and large incident angles as compared with the other cases. The maximum pressures and temperatures of the two cases of the octagonal front and the circular front are comparable. However, the circular front generates a longer high-pressure plateau. The flowfields of both circular front

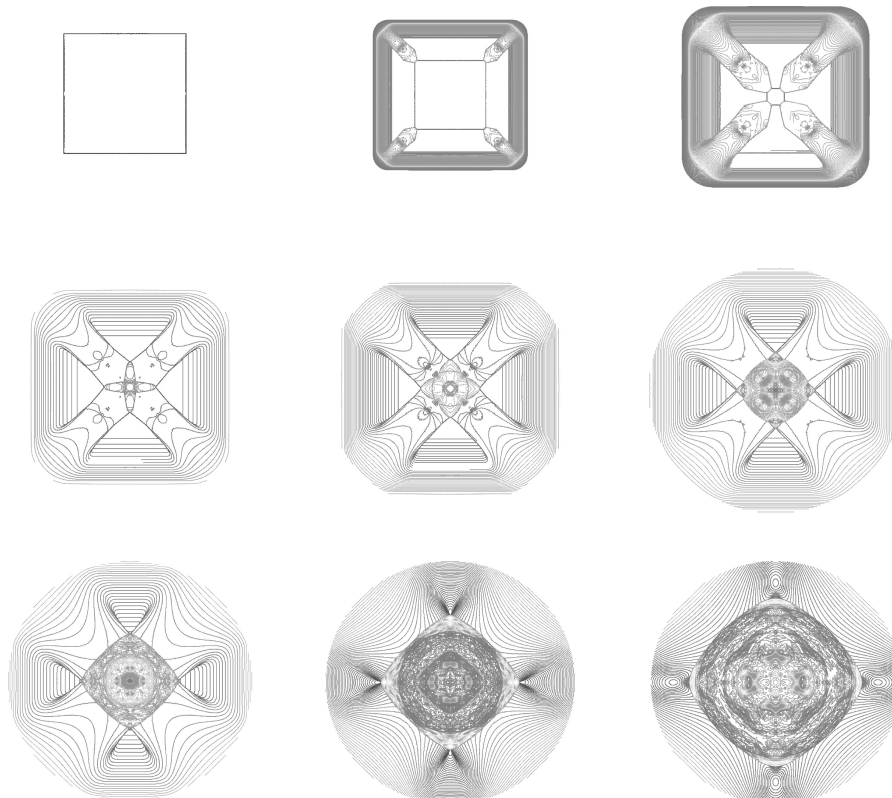


Fig. 17 Snapshots of pressure contours of a square implosion front at time = 0, 0.1, 0.2, 0.25, 0.3, 0.4, 0.5, 0.65, and 0.80.

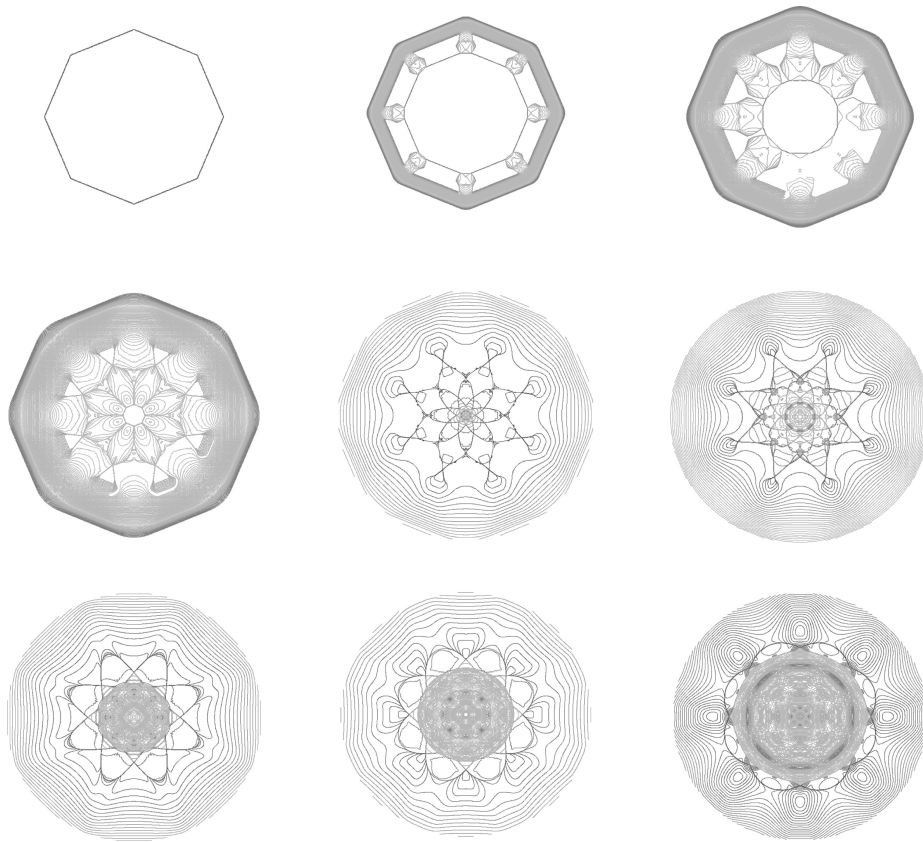


Fig. 18 Snapshots of pressure contours of an octagonal front at time = 0, 0.09, 0.18, 0.27, 0.315, 0.36, 0.495, 0.63, and 0.72.

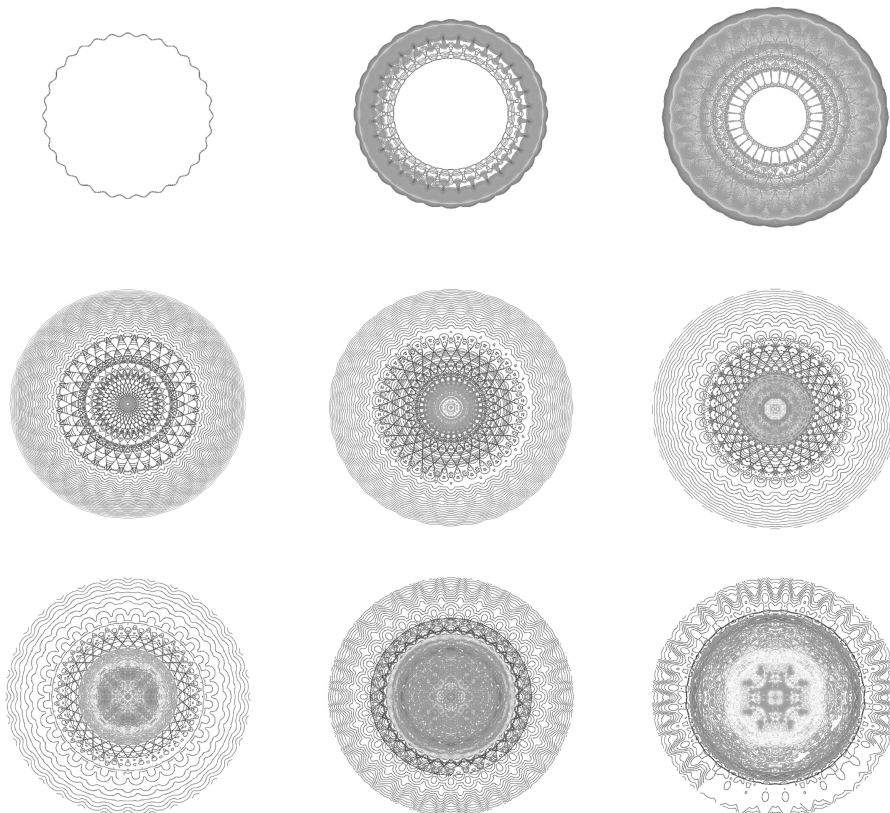


Fig. 19 Snapshots of pressure contours at time = 0, 0.09, 0.18, 0.27, 0.36, 0.45, 0.585, 0.72, and 0.90.

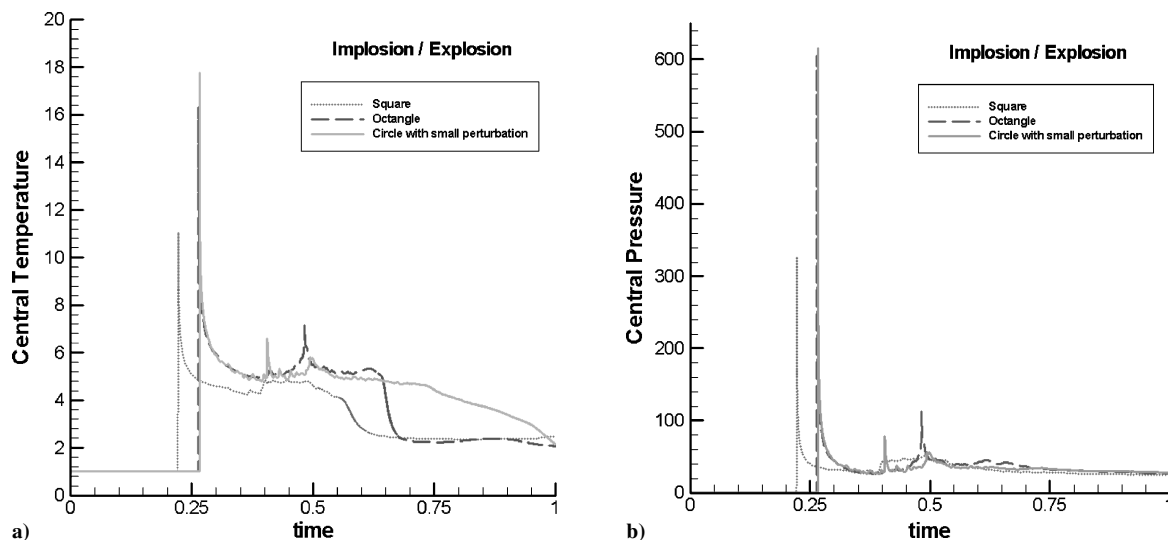


Fig. 20 Time histories at the focal point for the three nonreacting cases: a) temperature and b) pressure.

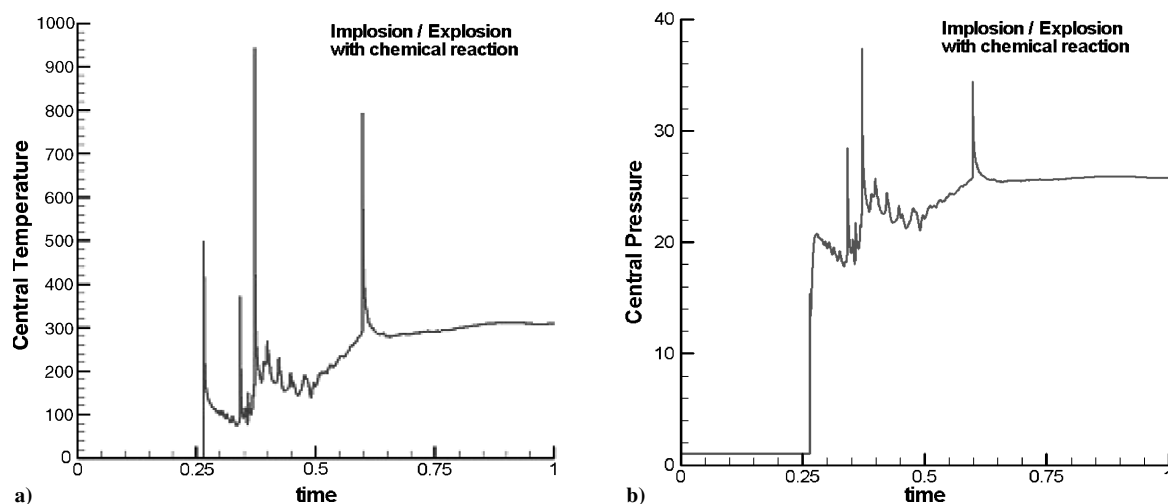


Fig. 21 Time histories at the focal point for the imploding reacting flow: a) temperature and b) pressure.

and the octagonal front show the secondary implosion similar to that in the one-dimensional results. The secondary implosion in the octagonal front case occurs later than that in the circular front case. The circular front case also shows a much weaker third implosion. On the other hand, the case of the square front does not show a clear secondary implosion. Figure 21 shows the histories of pressure and temperature at the focal point of a successful detonation initiation processes by imploding circular shock front with perturbations on the initial front surface. Similar to the one-dimensional results, consecutive shock implosions with a very strong secondary shock is evident. The overall pattern is much more complex as compared to the one-dimensional cases.

V. Conclusions

Direct numerical calculations of one- and two-dimensional implosions and explosions by using the space-time CESE method have been reported. In one-dimensional calculations, we found a two-implosion system with the secondary implosion caused by the interaction between the reflected primary shock and the imploding contact discontinuity. This double implosion shock system pushes the pressure and the temperature to be much higher than that created by the reflection of the primary shock wave only. Moreover, the reflected primary shock is greatly enhanced by the interaction. As a result, it quickly develops to be a robust detonation. In two-dimensional calculations, we focused on the calculations of poly-

gonal converging shock fronts. In the implosion phase, numerical images showed the regenerations of rotated and smaller polygonal forms. Time histories of flow variables at the focal point confirm the double implosion mechanism found in the one-dimensional results. These results also clearly demonstrate that the space-time CESE method is capable of catching salient features of complex implosion/explosion flows.

Acknowledgments

Financial support by the Office of Naval Research (ONR), Grant N00014-04-1-0559, monitored by Gabriel Roy, is greatly appreciated. We are indebted to J. E. Shepherd of Cal. Tech. for suggesting the general direction of this research work. Useful interactions with other members in the ONR Pulsed Detonation Engine program are also acknowledged.

References

- ¹Murray, S., Zhang, D., and Gerrard, K., "The Role of Energy Distribution on the Transmission of Detonation," International Colloquium on Control of Detonation Processes, Office of Naval Research, July 2000.
- ²Jackson, S., Grunthaler, M., and Shepherd, J., "Wave Implosion as an Initiation Mechanism for Pulse Detonation Engines," AIAA Paper 2003-4820, July 2003.
- ³Jackson, S., and Shepherd, J., "Initiation Systems for Pulse Detonation Engines," AIAA Paper 2002-3627, July 2002.

- ⁴Guderley, G., "Kugelige und Zylindrische Verdichtungsstosse in der Nake des Kugelmittelpunktes Lzw der Zylinderachse," *Luftfahrtforschung*, Vol. 19, No. 9, 1942, pp. 302–312.
- ⁵Taylor, G. I., "The Formation of a Blast Wave by a Very Intense Explosion, I. Theoretical Discussion," *Proceedings of the Physical Society. Section A*, Vol. 201, No. 1065, 1950, pp. 159–174.
- ⁶Taylor, G. I., "The Dynamics of the Combustion Products Behind Plane and Spherical Detonation Fronts in Explosives," *Proceedings of the Royal Society of London*, Vol. 200, No. 1061, 1950, pp. 235–247.
- ⁷Sedov, L. I., *Similarity and Dimensional Methods in Mechanics*, Cleaver Hume, London, 1959, Chaps. 4 and 5.
- ⁸Sharma, V. D., and Radha, C. H., "Similarity Solutions for Converging Shocks in a Relaxing Gas," *International Journal of Engineering Science*, Vol. 33, No. 4, 1995, pp. 535–553.
- ⁹Toque, N., "Self-Similar Implosion of a Continuous Stratified Medium," *Shock Waves*, Vol. 11, No. 3, 2001, pp. 157–165.
- ¹⁰van Dyke, M., and Guttman, A., "The Converging Shock Wave from a Spherical or Cylindrical Piston," *Journal of Fluid Mechanics*, Vol. 120, 1982, pp. 451–462.
- ¹¹Boyer, D. W., "An Experimental Study of the Explosion Generated by a Pressurized Sphere," *Journal of Fluid Mechanics*, Vol. 9, 1960, pp. 401–429.
- ¹²Friedman, M. P., "A Simplified Analysis of Spherical and Cylindrical Blast Waves," *Journal of Fluid Mechanics*, Vol. 11, 1961, pp. 1–15.
- ¹³Glass, I. I., and Sisljan, J. P., *Non-Stationary Flows and Shock Waves*, Oxford Science Publications, Oxford, 1994, Chap. 12.
- ¹⁴Baker, W. E., *Explosions in Air*, Wilfred Baker Engineering, San Antonio, TX, 1973, Chap. 7.
- ¹⁵Schwendeman, D. W., and Whitham, G. B., "On Converging Shock Waves," *Proceedings of the Physical Society. Section A*, Vol. 413, No. 1845, 1987, pp. 297–311.
- ¹⁶Brode, H. L., "Numerical Solution of Spherical Blast Waves," *Journal of Applied Physics*, Vol. 26, June 1955, pp. 766–775.
- ¹⁷Brode, H. L., "Blast Wave from a Spherical Charge," *Physics of Fluids*, Vol. 2, No. 2, 1959, pp. 217–229.
- ¹⁸Flores, J., and Holt, M., "Grimm's Method Applied to Underwater Explosions," *Journal of Computational Physics*, Vol. 44, No. 2, 1981, pp. 377–387.
- ¹⁹Glimm, J., "Solutions in the Large For Nonlinear Hyperbolic Systems of Equations," *Communications on Pure and Applied Mathematics*, Vol. 18, No. 4, 1965, pp. 697–715.
- ²⁰Charrier, P., and Tessieras, B., "A Front-Tracking Method Applied to Hyperbolic Systems of Nonlinear Conservation Laws," *SIAM Journal on Numerical Analysis*, Vol. 23, No. 2, 1986, pp. 461–472.
- ²¹Devore, C. R., and Oran, E. S., "The Stability of Imploding Detonations in the Geometrical Shock Dynamics (CCW) Model," *Physics of Fluids A*, Vol. 4, No. 4, 1992, pp. 835–844.
- ²²Oran, E. S., and Devore, C. R., "The Stability of Imploding Detonations: Results of Numerical Simulations," *Physics of Fluids*, Vol. 6, No. 1, 1996, pp. 369–380.
- ²³Boris, J. P., and Book, D. L., "Flux-Corrected Transport I. SHASTA, A Fluid Transport Algorithm That Works," *Journal of Computational Physics*, Vol. 11, No. 1, 1973, pp. 38–69.
- ²⁴Book, D. L., Boris, J. P., and Hain, K., "Flux-Corrected Transport II. Generalizations of the Method," *Journal of Computational Physics*, Vol. 18, No. 3, 1975, pp. 248–283.
- ²⁵Payne, R. B., "A Numerical Method for a Converging Cylindrical Shock," *Journal of Fluid Mechanics*, Vol. 2, 1956, pp. 185–200.
- ²⁶Lax, P. D., "Weak Solutions of Nonlinear Hyperbolic Equations and Their Numerical Computation," *Communication on Pure and Applied Mathematics*, Vol. 7, No. 1–2, 1954, pp. 159–193.
- ²⁷Falcovitz, J., and Birman, A., "A Singularities Tracking Conservation Laws Scheme for Compressible Duct Flows," *Journal of Computational Physics*, Vol. 115, No. 2, 1994, pp. 431–439.
- ²⁸Ben-Artzi, M., and Falvovitz, J., "A Second-Order Godunov-Type Scheme for Compressible Fluid Dynamics," *Journal of Computational Physics*, Vol. 55, No. 1, 1984, pp. 1–32.
- ²⁹Sod, G. A., "A Numerical Study of a Converging Cylindrical Shock," *Journal of Fluid Mechanics*, Vol. 83, 1977, pp. 785–794.
- ³⁰He, L. T., "Theoretical Determination of the Critical Conditions for the Direct Initiation of Detonations in Hydrogen-Oxygen Mixtures," *Combustion and Flame*, Vol. 104, No. 4, 1996, pp. 401–418.
- ³¹Menikoff, R., Lackner, K. S., and Bukiet, B. G., "Modeling Flows with Curved Detonation Waves," *Combustion and Flame*, Vol. 104, No. 3, 1996, pp. 219–240.
- ³²Yu, S. T., and Chang, S. C., "Treatments of Stiff Source Terms in Conservation Laws by the Method of Space-Time Conservation Element and Solution Element," AIAA Paper 97-0435, Jan. 1997.
- ³³Wang, B., and Yu, S.-T., "Direct Calculation of Spherical Detonation Initiation of H₂/O₂/Ar Mixtures by the CESE Method," AIAA Paper 2004-0793, Jan. 2004.
- ³⁴Yu, S. T., and Chang, S. C., "Applications of the Space-Time Conservation Element and Solution Element Method to Unsteady Chemically Reactive Flows," AIAA Paper 97-2099, June 1997.
- ³⁵Im, K.-S., Kim, C.-K., Yu, S. T., Chang, S. C., and Jorgenson, P. C. E., "Application of the CESE Method to Detonation with Realistic Finite-Rate Chemistry," AIAA Paper 2002-1020, Jan. 2002.
- ³⁶Park, S.-J., Yu, S. T., Lai, M.-C., Chang, S. C., and Jorgenson, P. C. E., "Direct Calculations of Stable and Unstable ZND Detonations by the Space-Time Conservation Element and Solution Element Method," AIAA Paper 99-0491, Jan. 1999.
- ³⁷Zhang, Z. C., Yu, S. T., and Chang, S. C., "A Space-time Conservation Element and Solution Element Method for Solving the Two- and Three-Dimensional Unsteady Euler Equations Using Quadrilateral and Hexahedral Meshes," *Journal of Computational Physics*, Vol. 175, No. 1, 2002, pp. 168–199.
- ³⁸Chang, S. C., "The Method of Space-time Conservation Element and Solution Element—A New Approach for Solving the Navier–Stokes and Euler Equations," *Journal of Computational Physics*, Vol. 119, No. 2, 1995, pp. 295–324.
- ³⁹Chang, S. C., Wang, X. Y., and Chow, C. Y., "The Space-Time Conservation Element and Solution Element Method: a New High-Resolution and Genuinely Multidimensional Paradigm for Solving Conservation Laws," *Journal of Computational Physics*, Vol. 156, No. 1, 1999, pp. 89–136.
- ⁴⁰Chang, S. C., Wang, X. Y., and To, W. M., "Application of the Space-Time Conservation Element and Solution Element Method to One-Dimensional Convection-Diffusion Problems," *Journal of Computational Physics*, Vol. 165, No. 1, 2000, pp. 189–215.
- ⁴¹Chang, S. C., "Courant Number Insensitive CE/SE Schemes," AIAA Paper 2002-3890, July 2002.
- ⁴²Oran, E. S., Young, T. R., Boris, J. P., and Cohen, A., "Weak and Strong Ignition, I, Numerical Simulations of Shock Tube Experiments," *Combustion and Flame*, Vol. 48, No. 2, 1982, pp. 135–148.
- ⁴³Dryer, F. L., "The Phenomenology of Modeling Combustion Chemistry, Section: 5.1: One- and Two-Step Global Mechanisms," *Fossil Fuel Combustion—A Source Book*, edited by W. Bartok and A. F. Sarofim, Wiley-Interscience, New York, 1991, Chap. 5.
- ⁴⁴McBride, B. J., and Gordon, S., "Computer Program for Calculation of Complex Chemical Equilibrium Compositions and Applications," NASA Reference Publication 1311, June 1996.
- ⁴⁵Toro, E. F., *Riemann Solvers and Numerical Methods for Fluid Dynamics*, 2nd ed., Springer, London, 1999, pp. 582–585.
- ⁴⁶Lu, T., Law, C. K., and Ju, Y., "Some Aspects of Chemical Kinetics in Chapman-Jouguet Detonation: Induction Length Analysis," *Journal of Propulsion and Power*, Vol. 19, No. 5, 2003, pp. 901–907.
- ⁴⁷Harten, A., Osher, S. J., Engquist, B. E., and Chakravarthy, S. R., "Some Results on Uniformly High-Order Accurate Essentially Non-Oscillatory Schemes," *Journal of Applied Numerical Mathematics*, Vol. 2, No. 3–5, 1986, pp. 347–377.
- ⁴⁸Hwang, P., Fedkiw, R. P., Merriman, B., Aslam, T. D., Karagozian, A. R., and Osher, S. J., "Numerical Resolution of Pulsating Detonation Waves," *Combustion Theory Modeling*, Vol. 4, No. 3, 2000, pp. 217–240.
- ⁴⁹Butler, D. S., "Converging Spherical and Cylindrical Shocks," Armament Research and Development Establishment, Ministry of Supply, Rept. 54/54, Fort Halstead, Kent, England, U.K., June 1954.
- ⁵⁰Stanyukovich, K. P., *Unsteady Motion of Continuous Media*, Pergamon, Oxford, 1960, p. 524, Chap. 5.
- ⁵¹de Neef, T., and Nechtman, C., "Numerical Study of the Flow Due to a Cylindrical Implosion," *Computational Physics*, Vol. 6, No. 2, 1978, pp. 185–202.
- ⁵²Takayama, K., Onodera, O., and Hoshizawa, Y., "Experiments on the Stability of Converging Cylindrical Shock Waves," *Theoretical and Applied Mechanics*, Vol. 32, No. 1, 1984, pp. 117–127.
- ⁵³Kleine, H., "Time Resolved Shadowgraphs of Focusing Cylindrical Shock Waves," Study Treatise at Stosswellenlabor, RWTH Aachen, Aachen, Germany, 1985.